Journal of Sound and Vibration (1999) **227**(4), 685–709
Article No. jsvi.1998.2104, available online at http://www.idealibrary.com on IDEAL

PREDICTION OF FLOW-INDUCED STRUCTURAL VIBRATION AND SOUND RADIATION USING ENERGY FLOW ANALYSIS

F. HAN, R. J. BERNHARD AND L. G. MONGEAU
1077 *Ray W. Herrick Laboratories, School of Mechanical Engineering, Purdue University, West Lafayette, IN* 47907, *U.S.A.*

(*Received* 3 *June* 1998, *and in final form* 30 *November* 1998)

The energy flow analysis method was used to predict the structural vibration response and the radiated sound power of a plate excited by wall pressure fluctuations under turbulent boundary layers, and separated–reattached flows. This method allows the spatially averaged energy density response to be calculated for non-uniform, distributed excitations while taking hydrodynamic flow/structural coupling effects into consideration. The power input was calculated using well known analytical models for the plate mechanical impedance and empirical models for the surface pressure cross-power spectral density and/or wave number–frequency spectral density. The Smol'yakov–Tkachenko model was used to estimate the fluctuating pressure field underneath turbulent boundary layer flows. The Corcos model was used to estimate the wall pressure field under non-uniform, separated–reattached flows. Experiments were performed in order to evaluate the energy flow model. A clamped plate installed in a quiet, low-speed wind tunnel was used. The wall pressure fluctuations, the plate vibration response, and the acoustic pressure radiated from the plate were measured. The energy flow analysis method was found to provide reasonably accurate predictions of the frequency-averaged transverse velocity response of the plate at high frequencies. The acoustic pressure radiated on the quiescent side of the plate was also predicted with comparable accuracy.

1. INTRODUCTION

Unwanted sound and vibration are often generated by pressure fluctuations acting on structures immersed in unsteady and/or turbulent flows. Examples include interior noise in automotive vehicles and aircraft, flow noise in submarines or ships, pipe vibrations, and external noise emission of propulsion systems, fluid-moving machinery and piping systems. In recent years, this problem has grown in importance for the case of automobiles as the engine, tires, and other noise sources have been reduced, and flow-induced vibration and noise have become comparatively more important.

0022–460X/99/440685 + 25 $30.00/0

Appropriate models for the wall pressure field are required in order to predict the response of extended structures to flow excitations. The pressure field beneath turbulent boundary layers (TBL) has been the focus of many previous investigations. The cross-power spectral density of the wall pressure was used to study the structural response in the 1950s and 1960s. The wave number–frequency spectrum of wall pressure fluctuations was later investigated by many researchers, with particular emphasis on the low wave number region of the spectrum [1]. Various empirical or semi-empirical models have been proposed for the wave number–frequency spectrum of wall pressure fields under turbulent boundary layers, including the Corcos model [2, 3], the Chase model [4, 5], the Ffowcs Williams model [6], and the Smol'yakov–Tkachenko model [7]. A comparison between these models was made by Borisyuk and Grinchenko [8], and also by Graham [9], for structural acoustics applications. These studies suggest that the Chase model and the Smol'yakov–Tkachenko model are in best agreement with experimental data for cases where the outer flow Mach number is low and the structures are relatively stiff. The use of these two models has been advocated for predictions at high frequencies, when the structural vibration response is dominated by resonant modes lying in the low wave number region of the wave number spectrum (i.e., a condition for which the "free" wave number of the structure is well below the "convective" wave number of the excitation). The use of the Corcos model for the same conditions was shown to lead to over-predictions of the structural response and the radiated sound power.

At low frequencies, a condition known as hydrodynamic coincidence exists for which the structural bending wave speed matches the convection speed of the wall pressure field over the structure. For this condition, the wave number corresponding to the resonance of the structure coincides with the wave number range where the wave number–frequency spectrum of the excitation is highest. The structural response is dominated by resonant components near the convective wave number. In this region, pressure amplitude predictions using any of the previously mentioned models are comparable.

Flow processes involving the separation and the reattachment of turbulent shear layers are encountered in many practical engineering applications. Separated–reattached flows may produce highly energized, organized turbulent flow and comparatively large surface pressure fluctuations. Yet, there are only a limited number of experimental investigations of the fluctuating surface pressure field beneath complex flows. Farabee and Casarella [10, 11] performed a series of measurements of the fluctuating wall pressure field produced by backward-facing and forward-facing step flows. Their results show that the separation–reattachment process produces large amplitude, low frequency pressure fluctuations. Coney *et al.* [12] measured the fluctuating pressure loading on automotive vehicle greenhouse surfaces, including the side glass window. Their study focused on the separated/vortex flow along the A-pillar area which produces high level pressures relative to regions of the vehicle where the outer flow is fully attached. Their study revealed certain characteristics of the wall pressure fields under the separated flow region and the reattachment flow region. Along with other researchers [13–15], they found that the use of a Corcos-type

model to describe the wall pressure fluctuations gives satisfactory results for this class of separated-reattached flows.

The design of safe, quiet engineered systems will be facilitated using first cut predictive models of the vibration and noise response of complex, flow-induced structural systems. The finite element method (FEM) has been used successfully for prediction of low frequency response. However, the finite element method is not yet practical for high frequencies due to prohibitive mesh size requirements and computational costs. Also, the deterministic approach used for traditional FEM is not appropriate at high frequencies where system variability is high. Therefore, high frequency response of complex structural/acoustic systems is generally predicted using statistical approaches such as the statistical energy analysis (SEA) method. For SEA, lumped parameters models are used to represent a continuous system. Therefore, a non-uniform loading on a substructure is usually space-averaged to obtain a single power input value [16]. For example, Wu *et al.* [15] investigated the case of a vehicle side glass window excited by turbulent flow. The side glass window panel was modelled as a single SEA element. In general, both separated/vortex flows and reattached flows exist on the surface of the side window. The authors did not take the inhomogeneity of the surface pressure field over the side glass window panel into consideration. Only the reattached flows were considered and the cross-correlation of wall pressure fluctuations was assumed to be homogeneous in space. The vibration and sound radiation of vehicle side glass windows was also studied by Strumolo using SEA [13]. In the study each flow region was treated separately in order to consider both the separated flow and the reattached flow. The contribution to the total power input from each flow region was assumed to be proportional to the corresponding wetted area.

An alternative high frequency, structural–acoustic analysis approach, referred to as the energy flow analysis method (EFA), has been developed recently [17, 18]. For a structure modelled using EFA, the input excitations can be multiple local forces [19] or a distributed loading [20] for which the spatial variation of the input can be modelled to match the spatial distribution of the source. Energy flow analysis can be used to predict the spatial variation of the space- and frequency-averaged vibratory energy level in built-up structures. The EFA method can be implemented using finite element methods, potentially enabling the use of common geometrical models and model development tools for both low frequency and high frequency predictions.

In this study, the application of the EFA method to flow-induced structural vibration problems is investigated. A method to calculate the power density input from presumably known dynamic load distributions and input mechanical impedance was developed [19, 20]. Using this power input method, EFA was used to predict the structural vibration and sound radiation of a clamped plate excited by (a) turbulent boundary layer flows; and (b) separated–reattached flows. The Smol'yakov–Tkachenko model was used to describe the fluctuating wall pressures for turbulent boundary layer flows. The Corcos model was used to describe the wall pressure field under separated and reattached flows. The contribution to the power input from different regions of the wave number

domain was evaluated. For the separated–reattached flow case, the non-uniform loading on the plate was fully considered in calculating the power density input. Experiments were performed in order to verify the accuracy of the proposed model.

2. THEORETICAL FORMULATION

2.1. WAVE NUMBER–FREQUENCY MODELS OF SURFACE PRESSURE FIELDS

For a turbulent flow grazing over an extended surface, the Corcos model of cross-power spectral density of the wall pressures at two separate locations $\mathbf{x}$ and $\mathbf{x}'$, $S_{\mathbf{xx}}$, can be written as

$$S_{\mathbf{xx}'} = \phi_{pp}(\omega)\mathrm{e}^{-\gamma_1|\omega\xi_1/U_c|}\,\mathrm{e}^{-\gamma_2|\omega\xi_2/U_c|}\,\mathrm{e}^{-\mathrm{j}\omega\xi_1/U_c}, \tag{1}$$

where $\phi_{pp}(\omega)$ is the auto-power spectral density, ω is the angular frequency, U_c is the turbulence convection speed, ξ_1 and ξ_2 are stream wise and span wise separations, respectively, and γ_1 and γ_2 are constants related to the coherence in the stream wise and span wise directions, respectively. The assumed time dependence factor for this model is $\mathrm{e}^{\mathrm{j}\omega t}$. The wave number–frequency spectrum can be obtained by performing a Fourier transform of equation (1) with respect to the two spatial coordinates. The result is

$$\phi(k_x, k_y, \omega) = \phi_{pp}(\omega)\frac{\gamma_1}{\pi[(k_x\omega/U_c - 1)^2 + \gamma_1^2]}\frac{\gamma_2}{\pi[(k_y\omega/U_c)^2 + \gamma_2^2]}, \tag{2}$$

where k_x and k_y are the stream wise and span wise wave number, respectively. This closed form expression, originally developed for turbulent boundary layers over flat plates, is widely used for various flows because of its mathematical simplicity. However, the use of this model provides satisfactory results only when the stream wise wave number k_x is in the neighborhood of the convective wave number ω/U_c. When k_x is in the subconvective range, the Corcos model tends to over-predict the subconvective spectrum significantly.

More recently, a refined version of the Corcos model has been developed. Smol'yakov and Tkachenko [7] measured the surface pressure cross-spectral density as a function of separation distance and boundary layer thickness. They performed a regression of the data using exponential curves. In contrast with the Corcos model, equation (1), the Smol'yakov–Tkachenko model includes a term of the form $\exp[-((\gamma_1\omega\xi_1/U_c)^2 + (\gamma_2\omega\xi_2/U_c)^2)^{1/2}]$. Fourier transform techniques were used to obtain the wave number–frequency spectral density. The resulting low wave number levels are lower, which is an improvement over the Corcos model, but they were still higher than experimental values. A correction was therefore added to the model to bring the model into agreement with experimental data. The final expression for the Smol'yakov–Tkachenko model in the wave number domain is

$$\phi(k_x, k_y, \omega) = \frac{1}{2\pi}\frac{\gamma_1}{\gamma_2}\phi_{pp}(\omega)A(\omega)h(\omega)\left(\frac{U_c}{\omega}\right)^2[F(k_x, k_y, \omega) - \Delta F(k_x, k_y, \omega)], \quad (3a)$$

where

$$A(\omega) = \gamma_1[1 - \mu U_c/\gamma_1 U_0\omega^* + (\mu U_c/\gamma_1 U_0\omega^*)^2]^{1/2}, \quad \omega^* = \omega\delta^*/U_0, \quad (3b, c)$$

$$h(\omega) = \left[1 - \gamma_1 mA/\gamma_2 n^2\sqrt{1 + A^2 - mn}\right]^{-1}, \quad m = (A^2 + 1)/(A^2 + 5n - 4), \quad (3d, e)$$

$$F(k_x, k_y, \omega) = [A^2 + (1 - U_c k_x/\omega)^2 + ((\gamma_1/\gamma_2)U_c k_y/\omega)^2]^{-3/2}, \quad (3f)$$

$$\Delta F(k_x, k_y, \omega) = \frac{1}{n}\left\{A^2 + 1 + \frac{n}{m}\left[\left(m - \frac{U_c k_x}{\omega}\right)^2 + \left(\frac{U_c k_y}{\omega}\right)^2 - m^2\right]\right\}^{-3/2}. \quad (3g)$$

In these relations, U_0 is the free-stream flow speed, δ^* is the boundary layer displacement thickness, μ and n are constants, $\mu = 0{\cdot}031$, $n = 1{\cdot}005$.

2.2. POWER INPUT CALCULATION

In order to use the EFA method for flow-induced vibration problems, a method must be developed to convert known or measurable information about the turbulent flow excitation into an input power form. The input power calculation must take the spatial coherence of the excitation over the surface of interest into consideration.

For a mechanical force applied to a structure, the power input is given by

$$\Pi_{in} = \tfrac{1}{2}\mathrm{Re}(Fv^*) = \tfrac{1}{2}|F|^2\ \mathrm{Re}(1/Z_m), \quad (4)$$

where F is the applied force, v is the velocity response, and Z_m is the impedance at the driving point. When the high frequency, spatially averaged response is considered, the relevant impedance of a finite system is known to approach that of an infinite system [21]. Therefore, the input impedance may be approximated by that of an infinite structure. The impedance of an infinite plate, which will be used in the following, is [22]

$$Z_\infty = 8(D\rho_s h_s)^{1/2}, \quad (5)$$

where D is the bending stiffness, ρ_s is the density of the plate and h_s is the plate thickness.

For a flow excitation, the load acting on the plate surface is a distributed, random pressure field. Han *et al.* [20] showed that the input power density at a position $\mathbf{x} = (x, y)$ on the plate can be expressed as

$$\pi_{in}(\mathbf{x}, \omega) = \frac{1}{8(D\rho_s h_s)^{1/2}}\mathrm{Re}\left(\int\int_S S_{\mathbf{x}\mathbf{x}'}\alpha_{\mathbf{x}\mathbf{x}'}\,\mathrm{d}\mathbf{x}'\right), \quad (6)$$

where S is the surface area of the plate, $S_{\mathbf{xx}'}$ is the cross-power spectral density between fluctuating pressures at positions $\mathbf{x}$ and $\mathbf{x}'$, and $\alpha_{\mathbf{xx}'}$ is given by

$$\alpha_{\mathbf{xx}'} = (1 + \mathrm{j}\eta/2)[H_0^{(1)}(k(1 + \mathrm{j}\eta/4)r) - H_0^{(1)}(\mathrm{j}k(1 + \mathrm{j}\eta/4)r)], \tag{7}$$

where $H_0^{(1)}$ is the Hankel function of first kind, k is the structural free wave number of the plate, η is the structural damping loss factor, and r is the distance between the position $\mathbf{x}$ and $\mathbf{x}'$.

The input power density can also be expressed in terms of the wave number–frequency spectral density of the wall pressure field if the wall pressure field is uniform. The input power density is

$$\pi_{in}(\mathbf{x}, \omega) = \frac{1}{8(D\rho_s h_s)^{1/2}} \mathrm{Re}\left[\int_{-\infty}^{\infty}\int_{-\infty}^{\infty} \phi(k_x, k_y, \omega)\mathrm{e}^{\mathrm{j}(k_x x + k_y y)}\alpha(\mathbf{x}, k_x, k_y)\,\mathrm{d}k_x\,\mathrm{d}k_y\right], \tag{8}$$

where $\phi(k_x, k_y, \omega)$ is the wave number–frequency spectral density of the fluctuating wall pressure field. The spatial Fourier transform convention $G(k_x) = \int_{-\infty}^{\infty} g(x)\mathrm{e}^{\mathrm{j}k_x x}\,\mathrm{d}x$ was used to obtain equation (8). The quantity $\alpha(\mathbf{x}, k_x, k_y)$ is defined as

$$\alpha(\mathbf{x}, k_x, k_y) = \int_0^{L_y}\int_0^{L_x} \alpha_{\mathbf{xx}'}\,\mathrm{e}^{-\mathrm{j}k_x x}\,\mathrm{e}^{-\mathrm{j}k_y y}\,\mathrm{d}x\,\mathrm{d}y, \tag{9}$$

where L_x and L_y are the dimensions of the plate.

This method of calculating the input power is referred to as the impedance method. Equation (6) can be used for both uniform and non-uniform loading. Equation (8) can only be used for uniform loading. For non-uniform loading, $S_{\mathbf{xx}'}$ is a function of position. Thus, the power input density in equation (6) is a function of position. Note that $\alpha_{\mathbf{xx}'}$ and $\alpha(\mathbf{x}, k_x, k_y)$ are also functions of position. Therefore, even for uniform loading, the power input still depends on position implicitly due to the presence of $\alpha_{\mathbf{xx}'}$ or $\alpha(\mathbf{x}, k_x, k_y)$.

2.3. ENERGY FLOW ANALYSIS

The premise of EFA is that the state of vibration can be represented by stored, dissipated and transferred energies. Assuming propagating plane waves, a governing equation for the energy density of a system can be derived by using a differential volume approach and the energy conservation principle for elastic media. For a thin, transversely vibrating plate, the governing equation is [17]

$$-(c_g^2/\eta\omega)\nabla^2\, e(x, y, \omega) + \eta\omega e(x, y, \omega) = \pi_{in}(x, y, \omega), \tag{10}$$

where e is the spatially and frequency averaged energy density, and c_g is the group velocity of flexural waves in the structure. Both the input power density and the energy density are functions of position. Thus, the spatial distribution of the energy density within the structure and the non-uniform distributed loading are taken into consideration by the model. For a plate with no energy loss at the

boundary, the flux of energy there is zero. Thus, the energy density e can be expanded into a Fourier series

$$e = \sum_{m,n=0}^{\infty} A_{mn} \cos\frac{m\pi x}{L_x} \cos\frac{n\pi y}{L_y}, \tag{11}$$

where the basis function $\cos(m\pi x/L_x)\cos(n\pi y/L_y)$ satisfies the energy boundary condition. Using Fourier analysis techniques, the power input can also be expanded in terms of the basis function as

$$\pi_{in}(x, y) = \sum_{m,n=0}^{\infty} B_{mn} \cos\frac{m\pi x}{L_x} \cos\frac{n\pi y}{L_y}, \tag{12}$$

where

$$B_{mn} = \int_0^{L_y} \int_0^{L_x} \pi_{in}(x, y) \cos\frac{m\pi x}{L_x} \cos\frac{n\pi y}{L_y}\, \mathrm{d}x\, \mathrm{d}y. \tag{13}$$

The solution of the energy flow equation (10) is then:

$$e = \sum_{m,n=0}^{\infty} B_{mn} \cos(m\pi x/L_x) \cos(n\pi y/L_y) / \{(c_g^2/\eta\omega)[(m\pi/L_x)^2 + (n\pi/L_y)^2] + \eta\omega\}. \tag{14}$$

The total energy can be approximated as twice the kinetic energy [17]. Thus, the average mean square velocity of the plate response can be obtained using

$$\bar{v}^2(\mathbf{x}) = e/\rho_s h_s, \tag{15}$$

where the over-bar denotes a time average.

2.4. SOUND RADIATION

The sound radiated from the plate can be calculated using the radiation efficiency method. The radiated sound power, $\bar{P}$, is given by [22]

$$\bar{P} = \sigma\rho c S\langle\bar{v}^2\rangle, \tag{16}$$

where σ is the radiation efficiency, ρ is the density of air, c is the speed of sound in air, and $\langle\ \rangle$ represents space-averaging over the whole plate. The radiation efficiency is defined as the ratio of the averaged sound power radiated per unit area of the vibrating surface (here, the rectangular plate) to the average sound power radiated per unit area of a large piston that is vibrating with the same average mean square velocity at high frequency. The radiation efficiency is difficult to calculate for rectangular plates. Maidanik [23] suggested the following empirical model:

$$\sigma = \begin{cases} 2\gamma(\lambda_c/L_x)^2 g_1(\alpha) + 2(1+\gamma)(\lambda_c/L_x)g_2(\alpha), & f < f_c, \\ \sqrt{L_x/\lambda_c}(1 + 1/\sqrt{\gamma}), & f \approx f_c, \\ (1 - f_c/f)^{-1/2}, & f > f_c, \end{cases} \tag{17a}$$

where

$$g_1(\alpha) = \begin{cases} (4/\pi^4)[(1-2\alpha^2)/\alpha(1-\alpha^2)^{1/2}], & f < f_c/2, \\ 0, & f > f_c/2, \end{cases} \tag{17b}$$

$$g_2(\alpha) = (1/4\pi^2)[(1-\alpha^2)\ln\{(1+\alpha)/(1-\alpha)\} + 2\alpha]/(1-\alpha^2)^{3/2} \tag{17c}$$

and $\alpha = (f/f_c)^{1/2}$; $\gamma = L_x/L_y$, f_c is the critical frequency and λ_c is the critical wave length.

In this study, the Smol'yakov–Tkachenko model was used to model the surface pressure field beneath the turbulent boundary layers for cases where the flow was attached to the panel surface. Equation (8) was used to calculate the power input from the flow to the structure. The Corcos model was used to model the wall pressure fields for separated–reattached flows. The power input from the flow to the structure was calculated using equation (6). The transverse velocity response of the structure was predicted using the energy flow analysis method. The sound power radiated from the structure was then calculated using equation (16).

3. EXPERIMENTAL METHODOLOGY

The experimental apparatus consisted of a rectangular steel plate which was mounted flush with the floor of a quiet flow wind tunnel test section, as shown in Figure 1. Sound from the panel was radiated into an anechoic enclosure below the plate. The plate was 47 cm long, 37 cm wide and 0·16 cm thick. The plate was attached to a rigid aluminum frame using evenly spaced screws. The fixture was designed to achieve a uniform clamped boundary condition on all four sides. The assembly was attached to an acoustically treated wooden enclosure, as shown in Figure 1. The enclosure was constructed using sand-filled double

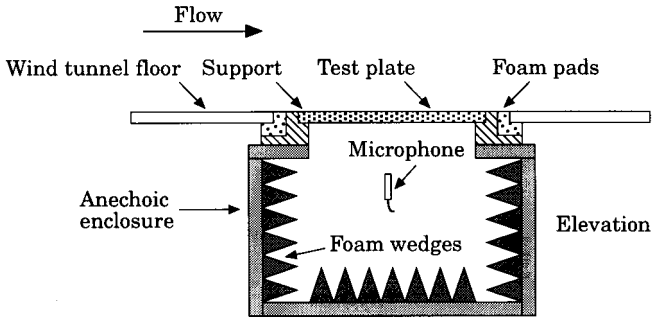

Figure 1. Experimental apparatus.

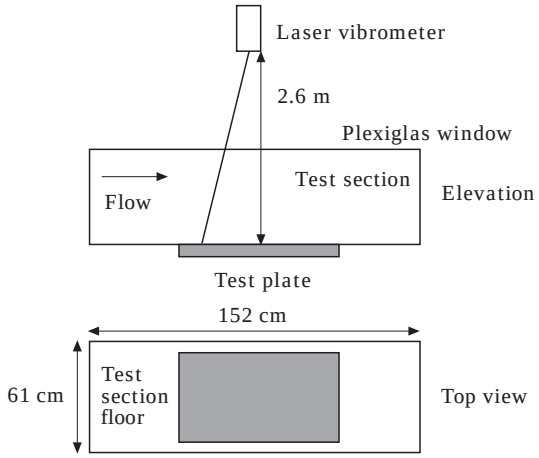

Figure 2. Schematic of the wind tunnel test section, the laser vibrometer and the test plate.

plywood walls and covered with foam wedges. An orifice in the top of the enclosure allowed sound to propagate from the plate into the enclosure. The assembly was mounted flush with the test section floor of the wind tunnel, with the longer plate dimension oriented in the stream wise direction. Foam pads were installed around the floor orifice and the aluminum frame to reduce the influence of the wind tunnel vibrations on the response of the plate when in operation. The plate configuration is shown in Figure 1 and Figure 2. The origin of the co-ordinate system was located in the left lower corner of the plate, with the x-axis along the stream wise direction and the y-axis along the span wise direction. The static pressure distribution over the test section of the wind tunnel was nearly uniform [25]. Therefore, the flow over the plate was considered an equilibrium turbulent boundary layer flow.

A scanning laser vibrometer was used to measure the plate velocity. The laser was mounted approximately 2·6 m above the center of the plate, as shown in Figure 2. The plate was coated with a special reflective paint containing suspended glass beads, which ensured good reflection of the laser beam. The plate response was measured at locations along a grid with 17 rows in the stream wise direction and 13 columns in the span wise direction, with a uniform spacing of 3 cm in both directions. The plate velocity was measured using the scanning function of the laser vibrometer at all 211 grid points for various flow speeds between 15·9 m/s and 44·7 m/s. The sound radiated from the plate into the enclosure was also measured using a condenser microphone. The co-ordinates of the microphone in the enclosure were (0·235 m, 0·185 m, −0·35 m).

A fence was later installed in the wind tunnel to create a separated–reattached flow. The fence was extended laterally across the test section upstream of the plate. Despite the possible effects from the boundary layer on the side walls and corner vortices, the flow was nearly two dimensional over the plate. The fence was 2·3 cm high. The angle between the fence and the test section floor was 60°. The location of the fence was 12·0 cm from the leading edge of the plate, as shown in Figure 3. The characteristic features of the flow are also schematically

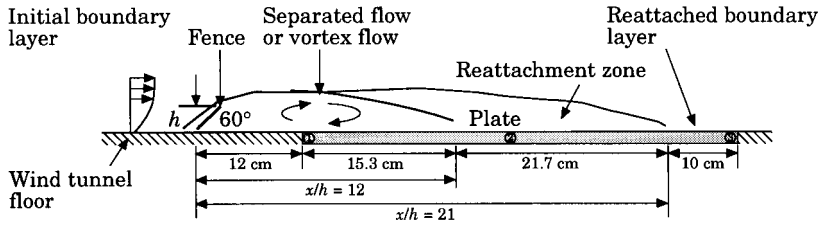

Figure 3. Flow over a fence: fence height $h = 2{\cdot}3$ cm; ① leading edge of the plate; ② center of the plate; ③ trailing edge of the plate.

TABLE 1

Measured loss factors of the plate

f (Hz)	81·3	141·9	188·8	240·0	246·2	372·5
η	0·0158	0·0085	0·0075	0·0063	0·0061	0·0030

illustrated in Figure 3. The flow field far upstream was an attached equilibrium boundary layer flow. The flow was tripped by the fence. A free-shear layer flow was thus created over the fence, with a strong re-circulated flow region near the wall immediately downstream of the fence. The flow was reattached to the wall at a distance of approximately 27·3 cm from the fence. Plate vibrations and acoustic pressures in the enclosure were also measured using the same method used for the TBL flow case.

Wall pressures were measured prior to the plate vibration experiments. A microphone array consisting of seven 3 mm condenser microphones was mounted flush with the test section floor. The auto- and cross-power spectral densities between the microphones were recorded. The microphone line array was placed in both the stream wise and the span wise directions. The surface pressure power spectral density, and the ordinary coherence function were obtained for a TBL flow over a flat, rigid plane, and for the separated–reattached flow described above. The spatial filtering effects caused by the finite size of the microphones were taken into consideration using the correction method suggested by Corcos [2].

The structural damping loss factor of the plate was experimentally determined using the half-power bandwidth method [16]. The transfer function between the velocity response of the plate and the impact force provided by a hammer was used to evaluate the value of modal damping. Results obtained for different excitation points were averaged in order to reduce the experimental error. The results for the first several natural frequencies are listed in Table 1. These damping loss factors were used in the EFA model. A loss factor of 0·002 was used for all frequencies above 37 Hz. The acoustic losses were not important compared with the structural damping in this case. Therefore, they were not included in the calculations.

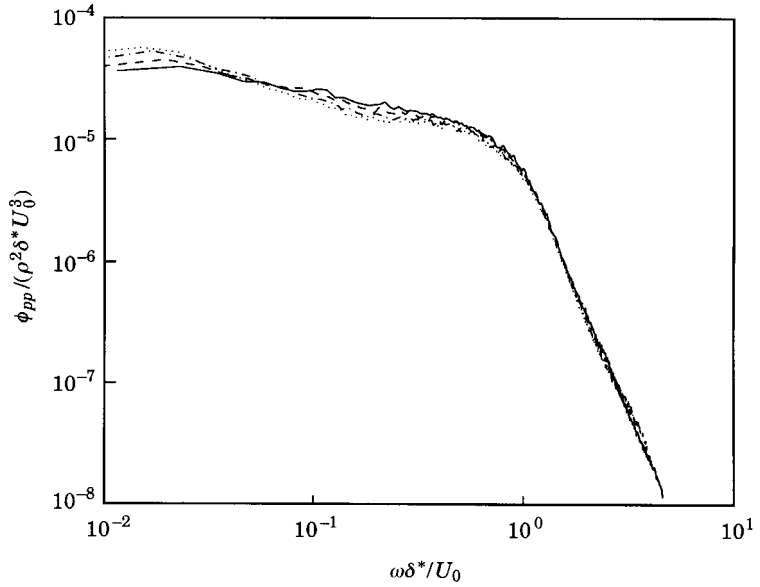

Figure 4. Turbulent boundary layer pressure spectral densities, scaled using outer flow variables: ——, $U_0 = 25{\cdot}3$ m/s; -----, $U_0 = 29{\cdot}9$ m/s; –·–·–, $U_0 = 34{\cdot}4$ m/s; ....., $U_0 = 39{\cdot}0$ m/s.

4. RESULTS AND DISCUSSION

4.1. PLATE EXCITED BY TURBULENT BOUNDARY LAYER FLOWS

The measured surface pressure auto-power spectral density is shown for a range of outer flow velocities in Figure 4. The spectra were scaled using a non-dimensional power spectral density parameter based on the outer flow velocity and outer boundary layer flow variables. The spectra collapsed into a single curve over the entire frequency range of interest. The boundary layer displacement thickness, measured using a hot-wire anemometer, was 2·9 mm [25]. The magnitude of the measured surface pressures is in relatively good agreement with similar data published elsewhere [1, 26]. The ordinary coherence function of the wall pressure field was calculated using the measured auto- and cross-power spectral densities. The coherence function is indicative of the correlation between pressure fluctuations at different locations. The coherence provides statistical information relative to the size, the convection speed, and the life time of large scale turbulent flow structures, or "eddies". The exponential spatial decay rates (see equation (1)) were obtained by regression. A decay rate of $\gamma_1 = 0{\cdot}11$ was obtained for the stream wise direction. Similarly, the decay rate for the span wise direction was estimated to be $\gamma_2 = 0{\cdot}70$. The convection velocity, U_c, was determined from the experimental data to be $U_c = 0{\cdot}65\ U_0$.

Surface pressure spectral density level predictions obtained using the Smol'yakov–Tkachenko model and the Corcos model are shown in Figure 5, as functions of the stream wise wave number. For these results, the frequency was 800 Hz and the free-stream velocity was 35·8 m/s. As stated earlier, the predicted

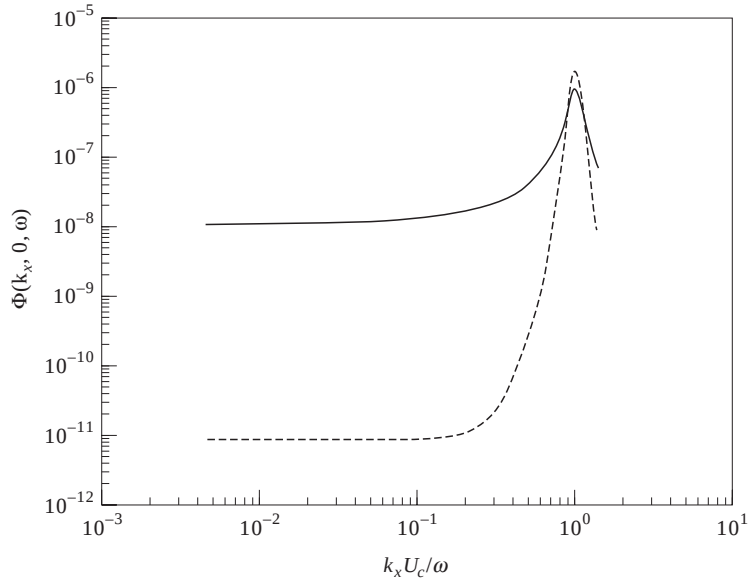

Figure 5. Calculated wave number–frequency spectral density using: ——, Corcos model; -----, Smol'yakov–Tkachenko model. $U_0 = 35{\cdot}8$ m/s, $f = 800$ Hz, $\gamma_1 = 0{\cdot}11$, $\gamma_2 = 0{\cdot}70$.

amplitudes in the sub-convective region are significantly lower when using the Smol'yakov–Tkachenko model than using the Corcos model.

The power input density to the plate was calculated using equation (8). The Smol'yakov–Tkachenko model was used for the surface pressure field. The wall pressure field was assumed uniform over the plate. The stream wise wave number transform of the pressure field and the factor $\alpha(\mathbf{x}, k_x, k_y)$, for $\mathbf{x} = (0{\cdot}23 \text{ m}, 0{\cdot}18 \text{ m})$ and $k_y = 0$, are shown in Figure 6 and Figure 7, respectively. Both are functions of frequency and of the stream wise wave

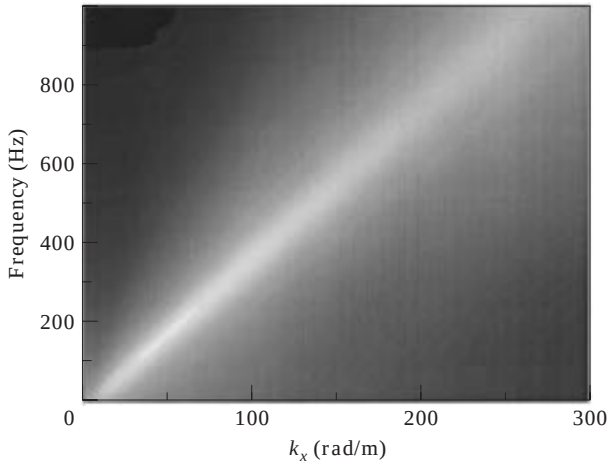

Figure 6. The wave number–frequency spectral density of the surface pressure field, $k_y = 0$.

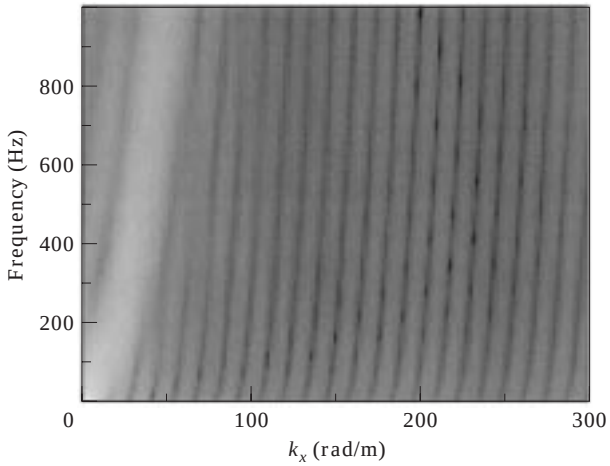

Figure 7. The wave number–frequency spectral density of $\alpha(\mathbf{x}, k_x, k_y)$, $\mathbf{x}$ = (0·23 m, 0·18 m) and $k_y = 0$.

number. The wave number transforms at a frequency of 800 Hz are shown in Figure 8. The factor $\alpha(\mathbf{x}, k_x, k_y)$ characterizes the wave number sensitivity of the structure. It exhibits a high peak at the structure free wave number. The region at and near this wave number is therefore the major sensitivity region of $\alpha(\mathbf{x}, k_x, k_y)$, as shown in Figure 8. Accordingly with previous investigations of the coupling between surface pressure field and modal response of plates, notably by Chandiramani [27] and Hwang and Maidanik [28], the major sensitivity lobe of $\alpha(\mathbf{x}, k_x, k_y)$ at 800 Hz was found to lie in the low-wave number region of the pressure wave number spectrum. By contrast, minor sensitivity lobes caused by a

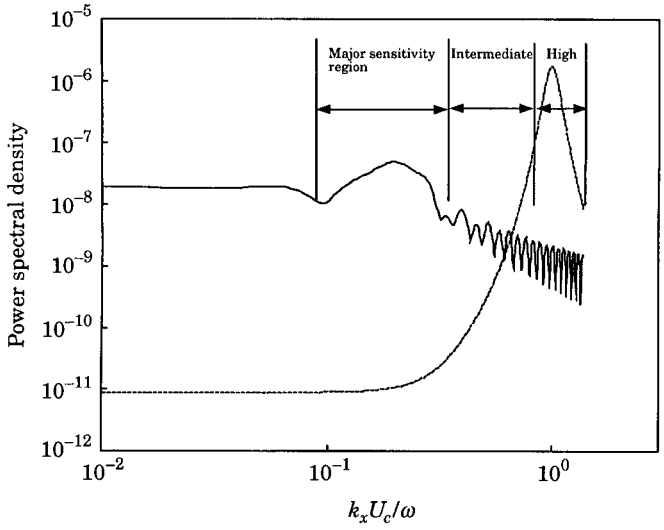

Figure 8. The coupling of the surface pressure field (------) and $\alpha(\mathbf{x}, k_x, k_y)$ (——) at 800 Hz, $\mathbf{x}$ = (0·23 m, 0·18 m) and $k_y = 0$.

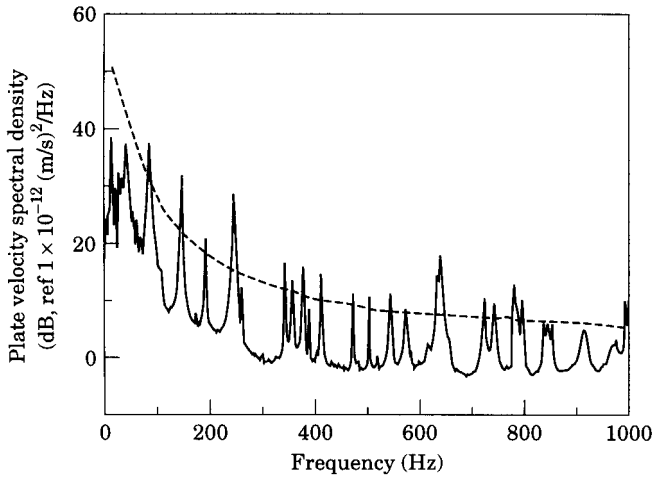

Figure 9. The plate velocity spectral density for TBL excitation: $U_0 = 35{\cdot}8$ m/s; ——, measured; -------, predicted.

discontinuity of the plate response at the edges coincide with the high convective components of the surface pressure spectrum. The source–filter interaction between the two functions is known as an "edge" interaction. The magnitudes of the minor lobes are determined by the plate boundary conditions. A panel with finite value of displacement at boundaries has stronger minor sensitivity lobes than a panel with simply supported or clamped boundary conditions, since such a panel has no displacement along the boundary [28]. The boundary condition of the plate was assumed to be non-reflective in the impedance method. Therefore, the predicted plate response has a higher high-wave number sensitivity than finite panels with simply supported or clamped boundary conditions. Thus, the contribution of the high-wave number region to the power input for a clamped plate is overestimated using the impedance method. However, the major sensitivity region and the intermediate region cover a much wider wave number range than the high wave number region. The contribution from the major sensitivity and intermediate wave number regions is dominant in the total power input to the plate. Errors introduced by the impedance method are thus considered insignificant.

At low frequency, around 50 Hz, the major sensitivity region of $\alpha(\mathbf{x}, k_x, k_y)$ and the convective peak of the pressure field coincide, as shown in Figures 6 and 7. The contribution from the major sensitivity region will be dominant relative to the contribution from the minor lobes which lie in the super-convective region of the surface pressure spectrum.

The measured and predicted plate velocity spectral densities for a flow speed of 35·8 m/s are shown in Figure 9. The results shown were averaged over the plate surface. At low frequencies, the plate response is over-predicted. In this region, the assumptions of the impedance method of input power estimation are not met since there are few resonant modes and the real impedance does not approach the impedance of an infinite plate. At high frequencies, the EFA

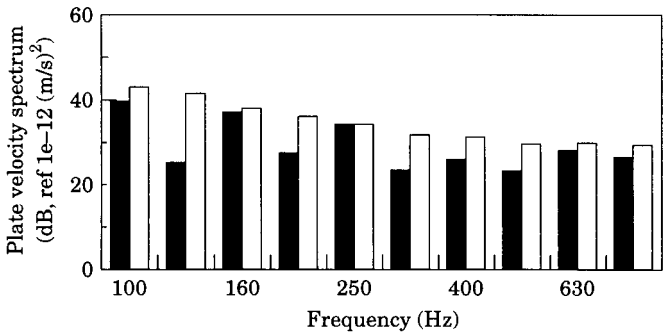

Figure 10. The plate vibration velocity spectrum for TBL excitation: $U_0 = 35{\cdot}8$ m/s; ■, measured; □, predicted.

prediction provides a good indication of the frequency-averaged response of the structure. This is further demonstrated in Figure 10, where the spatially averaged response is shown in one-third octave bands. In the 125 Hz and 315 Hz bands, there are few resonant modes. Therefore, there are differences between measured and predicted results. As the frequency is increased and especially in frequency bands where the modal density is high, the differences between the measured and predicted values are smaller.

The "measured" and the predicted vibrational energy density distribution of the plate at $x = 0{\cdot}25$ m in the one-third octave band centered at 800 Hz for a flow speed of 35·8 m/s is shown in Figure 11. The total energy of the plate equals to the kinetic energy plus the potential energy. The "measured" kinetic energy density was deduced from the measured velocity response, and the density and thickness of the plate. Since the potential energy was difficult to measure, the total energy density was assumed to be twice the kinetic energy density. This assumption breaks down near plate boundaries where the kinetic energy is zero whereas the potential energy is non-zero for the clamped plate. The difference between the predicted and "measured" energy densities near boundaries is thus an artificial effect. In the central region of the plate where the kinetic energy approximately equals to the potential energy, there is a good agreement between predicted and space-averaged "measured" results.

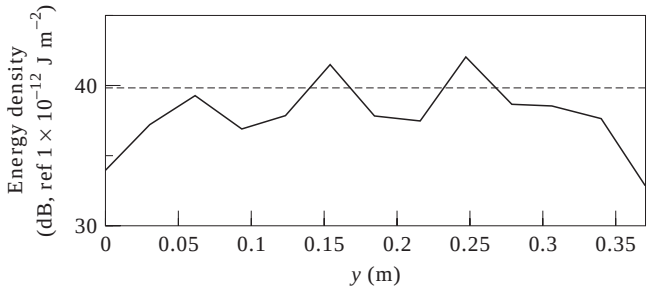

Figure 11. The energy density distribution in the plate at $x = 0{\cdot}25$ m in the 800 Hz one-third octave band, $U_0 = 35{\cdot}8$ m/s: ——, measured; -----, predicted.

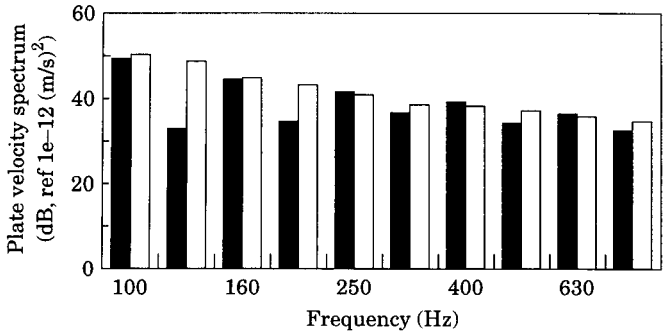

Figure 12. The plate vibration spectrum for TBL excitation, $U_0 = 44{\cdot}7$ m/s: ■, measured; □, predicted.

The measured and predicted spatially averaged frequency responses of the plate for a flow speed of 44·7 m/s are shown in Figure 12. The agreement is good, especially at high frequencies where the modal density is high. As expected, the plate vibration levels are higher than for 35·8 m/s.

Unfortunately, the radiated acoustic pressure was contaminated by wind tunnel background noise, due to the comparatively low excitation levels. Therefore, no results are shown here.

4.2. PLATE EXCITED BY SEPARATED–REATTACHED FLOWS

The characteristic features of the flow over the fence, as revealed using the smoke flow visualization, are schematically illustrated in Figure 3. The flow field upstream of the fence is an attached equilibrium boundary layer flow. When the attached flow encounters the fence, it is forced to separate from the wall. The tripped flow features a free-shear layer, a recirculated flow region with separation and reattachment zones, and possibly other secondary flows near the

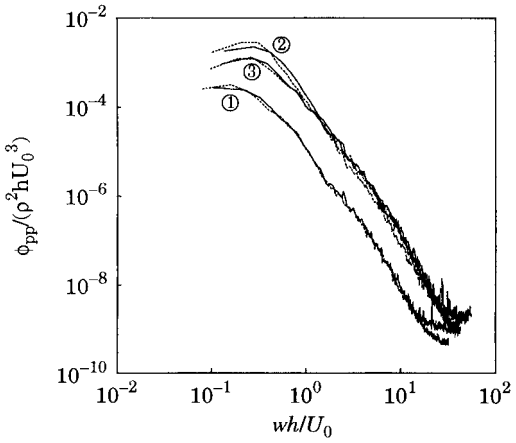

Figure 13. Wall pressure spectral densities scaled on outer flow variables and the fence height: ——, 26·8 m/s; ------, 35·8 m/s. ① leading edge of the plate; ② center of the plate; ③ trailing edge of the plate.

side-walls of the test section. The reattached flow evolves back to an equilibrium boundary layer as vortices are convected downstream. The reattachment region is located approximately at $12 < x/h < 21$, which is approximately the central region of the test plate. Three flow regions were therefore present over the surface of the plate: a separated/vortex flow, a reattachment zone, and a reattached flow. Their sizes over the plate were 15·3 cm, 21·7 cm and 10·0 cm along the stream wise direction, respectively.

The flow speed ranged from 20 m/s to 45 m/s, corresponding to a Reynolds number range based on fence height from $1{\cdot}07 \times 10^4$–$5{\cdot}31 \times 10^4$. Figure 13 shows the wall pressures measured at three different locations, for two different flow speeds. Non-dimensional pressure and frequency parameters were formed using free-stream flow velocity and the height of the fence as velocity and length scales, respectively. For a certain position, the wall pressure spectra of different flow speeds collapsed into a single curve. The wall pressure fluctuations are therefore produced by large turbulent structures with length scales of the order of the fence height. The spectral levels are significantly increased compared with the turbulent boundary layer case, especially at low frequencies. The separated–reattached flow produces highly energized, organized turbulent flows and large pressure fluctuations. These characteristics are typical, and they are similar to those reported by Farabee and Casarella [10, 11] who studied the surface pressure field behind backward-facing step flow and forward-facing step flow. The amplitude of the wall pressure fluctuations peaks at the center of the plate in the reattachment zone. Near the leading edge of the plate, in the re-circulated separated/vortex flow region, the level of the wall pressure spectral density is much lower. Near the trailing edge of the plate, in the reattached boundary layer

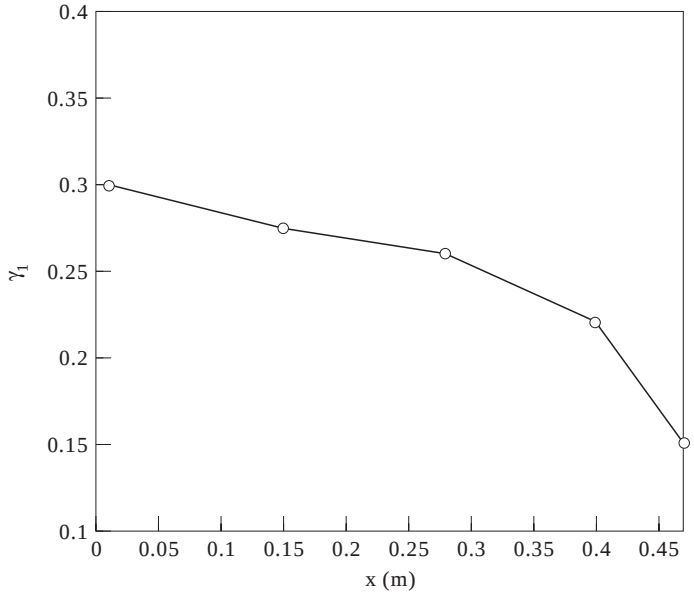

Figure 14. Measured results of decay rate of stream wise coherence over the plate.

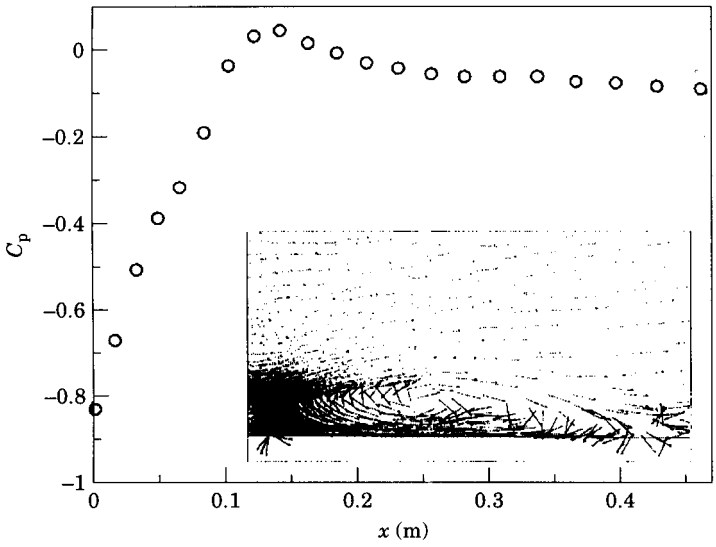

Figure 15. Computed result of static pressure coefficient distribution over the plate and velocity field behind the fence.

flow region, the low frequency content of the wall pressures was lower than that in the reattachment zone.

The coherence spectra under the separated–reattached flow field were also obtained for different flow speeds. Figure 14 shows the decay rate γ_1 of the stream wise coherence as a function of position over the plate. The pressure field in the vortex flow region and the reattachment zone were not as coherent as the pressure field for the TBL flow, for which the stream wise decay rate was 0·11. The flow was more coherent downstream of the reattachment point, indicating that the flow is evolving back to an equilibrium flow there. The decay rate in the span wise direction was found to be approximately 0·58 for all flow conditions over the plate.

The turbulence convection velocity was found to be $U_c = 0{\cdot}50\ U_m$ for the separated/vortex flow as opposed to $U_c = 0{\cdot}65\ U_m$ for the attached flow, where U_m is the local flow speed [10]. The local speed is related to the free stream flow speed by $U_m = U_0\sqrt{1 - C_p}$, where C_p is the static pressure coefficient. The static pressure distribution was obtained using computational fluid dynamics (CFD) methods. The static pressure coefficient over the plate was calculated using the commercially available software FLUENT [29]. The computed stream wise pressure coefficient and the velocity field are shown in Figure 15. The flow over the fence was assumed to be two-dimensional, and incompressible. The computational domain included 1429 nodes and 2583 triangular elements.

All regions of the plate contributed to the input power significantly. The non-uniformity of the surface pressure field over the plate was therefore taken into account. The power input densities at 48 evenly distributed grid points over the plate were calculated using the impedance method, equation (6). Measured data were used for the coherence within each flow region. The coherence between

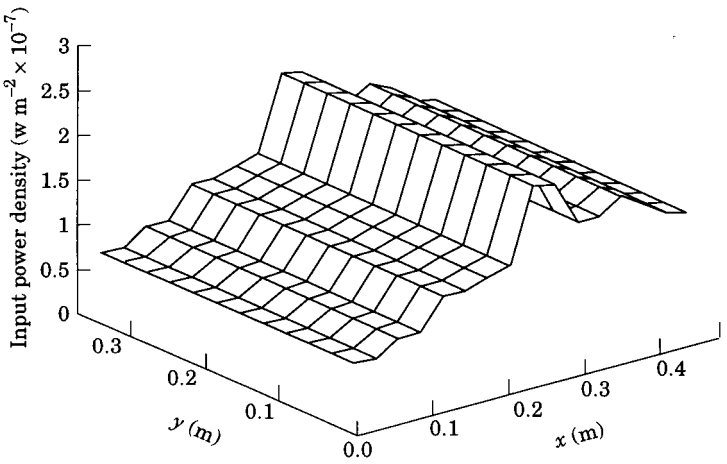

Figure 16. Input power density distribution over the plate at 500 Hz.

different flow regions, which was not measured, was assumed to be zero. This assumption appears to be reasonable since the main flow characteristics in different flow regions did not appear to be related. The input power density distribution over the plate at 500 Hz for a flow velocity of 35·8 m/s is shown in Figure 16. The power input amplitude was the largest in the reattachment zone.

The plate vibration was then obtained by solving the EFA equation using Fourier techniques. The non-uniform distributed input power was accounted for

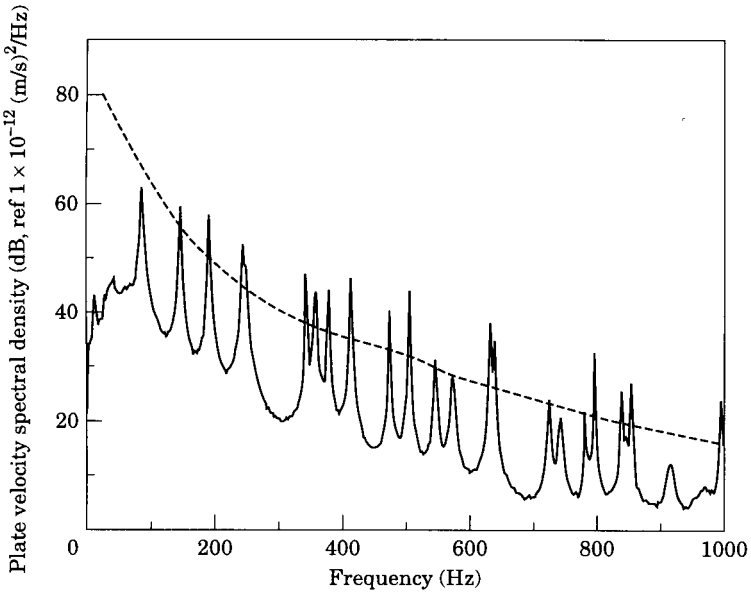

Figure 17. The plate velocity spectral density for the case of separated–reattached flow excitation, U_0 = 35·8 m/s: ——, measured; ------, predicted.

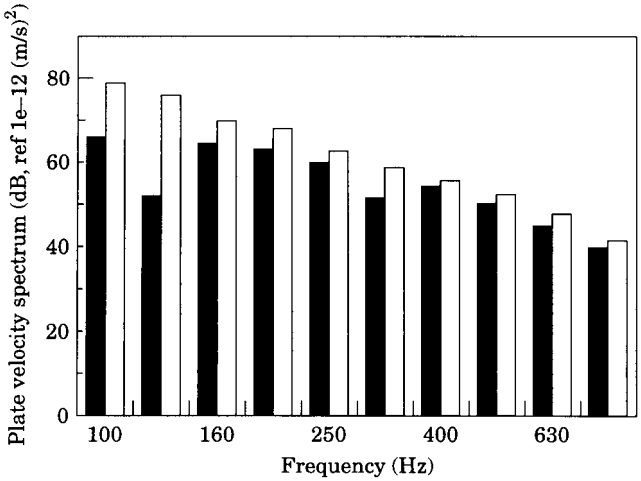

Figure 18. The measured and predicted plate vibration spectrum for separated–reattached flow excitation, U_0 = 35·8 m/s: ■, measured; □, predicted.

in the calculations through the use of equation (12). The EFA predictions are compared with the measured plate velocity for a free-stream flow velocity of 35·8 m/s in Figure 17. The one-third octave band vibration levels are shown in Figure 18. The vibration level is much higher than that for the turbulent boundary layer flow. The discrepancies at low frequencies are still primarily due to low modal density of the plate. The results for a free-stream flow speed of 44·7 m/s are shown in Figure 19. Again, the agreement improves as the frequency (and thus the modal density of the structure) is increased.

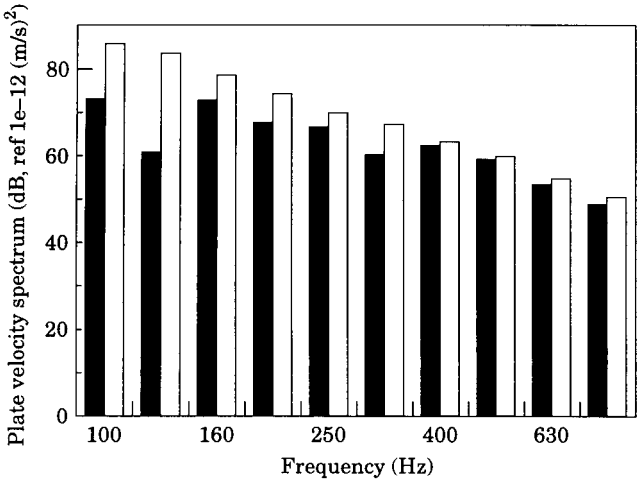

Figure 19. The measured and predicted plate vibration spectrum for separated–reattached flow excitation, U_0 = 44·7 m/s: ■, measured; □, predicted.

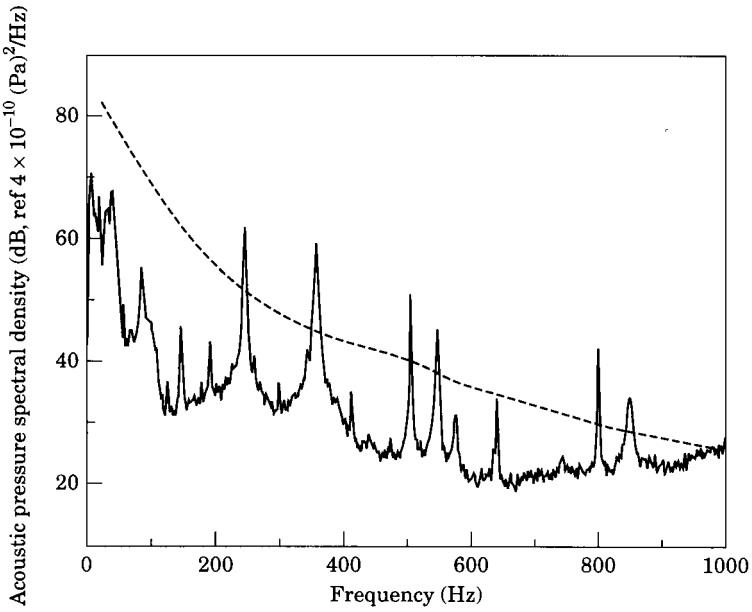

Figure 20. The acoustic pressure spectral density for separated–reattached flow excitation, $U_0 = 35{\cdot}8$ m/s: ——, measured; -----, predicted.

The radiated sound power was calculated using equation (16). By assuming the radiated acoustic pressure was uniformly distributed over a semi-spherical surface, the acoustic pressure at a single point in the enclosure below the plate was calculated simply by dividing the sound power by the semi-spherical surface area. The acoustic pressure radiated from the plate was much higher than the

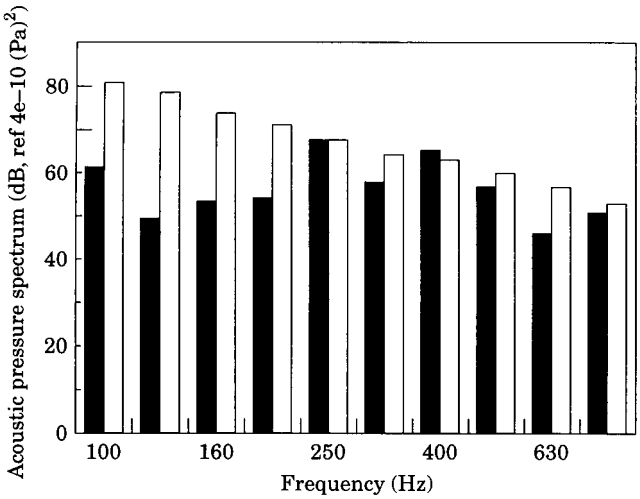

Figure 21. The acoustic pressure spectrum for separated–reattached flow excitation, $U_0 = 35{\cdot}8$ m/s: ■, measured; □, predicted.

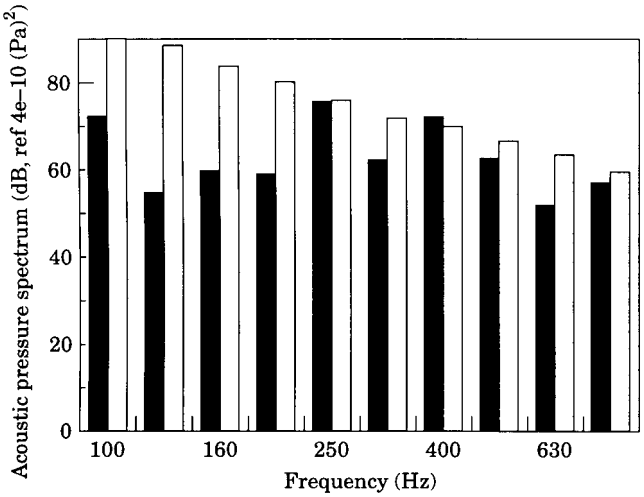

Figure 22. The acoustic pressure spectrum for separated–reattached flow excitation, $U_0 = 44{\cdot}7$ m/s: ■, measured; □, predicted.

background noise level for this case. The predictions, along with the measured pressures, are shown in Figure 20 for 35·8 m/s flow. The pressure levels in one-third octave bands are shown in Figures 21 and 22 for 35·8 m/s flow and 44·7 m/s flow, respectively. The modal density of the measured pressure is very low since only odd–odd modes of the plate are efficient in radiating sound. Therefore, there is a difference between the EFA predictions and measured acoustic pressures in one-third octave bands.

5. CONCLUSIONS

In this investigation, the energy flow analysis method was applied to the problem of flow-induced sound and vibration of a clamped, rectangular, homogeneous plate. The power density input was calculated using the impedance of an infinite plate and the cross-power spectral density or the wave number–frequency spectral density of the fluctuating pressure field. The method was verified experimentally for two different flow conditions: turbulent boundary layer flows and separated–reattached flows. The spatial distribution of the non-uniform loading on the plate was accounted for in the separated–reattached flow case. The predictions provided accurate approximations of the frequency and spatially averaged response of the plate at high frequencies over a range of flow speeds. The sound radiation prediction was also reasonably good. This study suggests that the EFA method is a useful tool for predictions of the behavior of complex, flow-excited structural/acoustic systems.

REFERENCES

1. W. K. BLAKE 1986 *Mechanics of Flow-induced Sound and Vibration*. New York: Academic Press; **I** and **II**.
2. G. M. CORCOS 1963 *Journal of the Acoustical Society of America* **35**, 192–199. Resolution of pressure in turbulence.
3. G. M. CORCOS 1967 *Journal of Sound and Vibration* **6**, 59–70. The resolution of turbulent pressures at the wall of a boundary layer.
4. D. M. CHASE 1980 *Journal of Sound and Vibration* **70**, 29–67. Modelling the wave-vector–frequency spectrum of turbulent boundary layer wall pressure.
5. D. M. CHASE 1987 *Journal of Sound and Vibration* **112**, 125–147. The character of the turbulent wall pressure spectrum at subconvective wavenumbers and a suggested comprehensive model.
6. J. E. FFOWCS WILLIAMS 1982 *Journal of Fluid Mechanics* **125**, 9–25. Boundary-layer pressures and the Corcos model: a development to incorporate low-wavenumber constraints.
7. A. V. SMOL'YAKOV and V. K. TKACHENKO 1992 *Soviet Physics-Acoustics* **37**, 627–631. Model of a field of pseudosonic turbulent wall pressures and experimental data.
8. A. O. BORISYUK and V. T. GRINCHENKO 1997 *Journal of Sound and Vibration* **204**, 213–237. Vibration and noise generation by elastic elements excited by a turbulent flow.
9. W. R. GRAHAM 1997 *Journal of Sound and Vibration* **206**, 541–365. A comparison of models for the wavenumber-frequency spectrum of turbulent boundary layer pressures.
10. T. M. FARABEE and M. J. CASARELLA 1984 *Journal of Vibration, Acoustics, Stress, and Reliability in Design* **106**, 343–350. Effects of surface irregularity on turbulent boundary layer wall pressure fluctuations.
11. T. M. FARABEE and M. J. CASARELLA 1986 *Journal of Vibration, Acoustics, Stress, and Reliability in Deisgn* **108**, 301–307. Measurements of fluctuating wall pressure for separated reattached boundary layer flows.
12. W. B. CONEY, J. Y. HER and J. A. MOORE 1997 AD-Vol. 53-1, *Fluid–Structure Interaction, Aeroelasticity, Flow-Induced Vibration and Noise*, Volume 1, ASME 1997, 411–418. Characterization of the wind noise loading of a production automobile greenhouse surfaces.
13. G. S. STRUMOLO 1997 *SAE paper* 971921. The wind noise modeler.
14. B. MASSON, P. NELSON and E. NIENALTOWSKA 1992 *DGLR/A1AA Aeroacoustic Conference, Aachen, Germany*. Development of a prediction method for the noise generated by a separated flow and transmitted by a flexible surface.
15. S. F. WU 1997 *Journal of Vibration and Acoustics* **119**, 557–562. Noise transmission through a vehicle side window due to turbulent boundary layer excitation.
16. R. H. LYON and R. G. DEJONG 1995 *Theory and Application of Statistical Energy Analysis*. Butterworth-Heinemann.
17. O. M. BOUTHIER and R. J. BERNHARD 1995 *Journal of Sound and Vibration* **182**, 149–164. Simple models of the energetics of transversely vibrating plates.
18. Y. LASE, M. N. ICHCHOU and L. JEZEQUEL 1996 *Journal of Sound and Vibration*, **192**, 281–305. Energy flow analysis of bars and beams: theoretical formulation.
19. F. HAN, R. J. BERNHARD and L. G. MONGEAU 1997 *Journal of Sound and Vibration* **208**, 841-859. Energy flow analysis of vibrating beams and plates for discrete random excitations.
20. F. HAN, L. G. MONGEAU and R. J. BERNHARD 1998 *Journal of Fluids and Structures* **12**, 315–333. Energy flow analysis of beams and plates for random distributed loading.
21. L. CREMER, M. HECKL and E. E. UNGAR 1988 *Structure-Borne Sound*. Berlin and New York: Springer-Verlag.

22. F. FAHY 1985 *Sound and Structural Vibration: Radiation, Transmission and Response*. London: Academic Press.
23. G. MAIDANIK 1962 *Journal of the Acoustical Society of America* **34**, 809–826. Response of ribbed panels to reverberant acoustic field.
24. M. J. CROCKER and A. J. PRICE 1963 *Journal of Sound and Vibration* **9**, 469–486. Sound transmission using statistical energy analysis.
25. D. V. BROWN and L. MONGEAU 1995 *Ray W Herrick Laboratories, Purdue University, Internal Report* 204. The design, construction, and validation of a small, low speed, quiet wind tunnel with application to noise from the flow over a cavity.
26. M. K. BULL 1967 *Journal of Fluid Mechanics* **28**, 719–754. Wall-pressure fluctuations associated with subsonic turbulent boundary layer flow.
27. K. L. CHANDIRAMANI 1977 *Journal of the Acoustical Society of America* **61**, 1460–1470. Vibration response of fluid-loaded structure to low-speed flow noise.
28. Y. F. HWANG and G. MAIDANIK 1990 *Journal of Sound and Vibration* **142**, 135–1152. A wave number analysis of the coupling of a structure mode and flow turbulence.
29. C. J. FREITAS 1995 *Journal of Fluids Engineering* **117**, 208–218. Perspective: selected benchmarks from commercial CFD codes.

APPENDIX: NOMENCLATURE

c	speed of sound in fluid
c_g	group speed of waves
D	bending stiffness
e	energy density
f	frequency
f_c	critical frequency
F	force in frequency domain
h	fence height
h_s	plate thickness
$H_0^{(1)}$	Hankel function of first kind
k	structural free wave number
k_x	stream wise wave number
k_y	span wise wave number
$\bar{P}$	sound power
r	$r = \lvert\mathbf{x}-\mathbf{x}'\rvert$
S	plate surface area
$S'_{\mathbf{xx}}$	cross-power spectral density of wall pressure field
t	time
U_0	free-stream flow speed
U_c	convection speed of turbulence
U_m	local flow speed
v	structural vibration velocity
x	x-coordinate
y	y-coordinate
Z_m	mechanical impedance of the driving point of a structure
Z_∞	mechanical impedance of an infinite structure
$\mathbf{x}$	$\mathbf{x} = (x, y)$
δ	boundary layer thickness
δ^*	boundary layer displacement thickness

$\phi_{pp}(\omega)$	auto-power spectral density
$\phi(k_x, k_y, \omega)$	wave number-frequency spectral density of wall pressure field
γ_1	decay rate of stream wise coherence
γ_2	decay rate of span wise coherence
η	structural damping loss factor
λ_c	critical wavelength
π_{in}	input power density
Π_{in}	power input
ρ_s	density of structures
ρ	density of fluid
σ	radiation efficiency
ω	angular frequency
ξ_1	stream wise distance
ξ_2	span wise distance
$< >$	spatial averaging
—	time averaging